Use of a charge coupled device camera for low-angle elastic light scattering

Fabio Ferri
Istituto di Scienze Matematiche, Fisiche, Chimiche and INFM (Istituto Nazionale di Fisica della Materia) - University of Milan at Como via Lucini, 3-22100 Como, Italy

(Received 19 December 1996; accepted for publication 28 February 1997)

A charge coupled device (CCD) camera has been successfully used to implement a low-angle elastic light scattering setup. A novel optical detection layout brings all the light scattered by the sample directly onto the CCD, optimizing the instrument sensitivity. The detectable angular range covers ~ 2 decades, from $\sim 0.1°$ to $\sim 10°$. The calibration of the instrument, as well as the estimate of its sensitivity, accuracy, dynamic range and linearity, can be carried out by using single pinholes. Experimental results from pinholes and diluted suspensions of polystyrene spheres are presented. © *1997 American Institute of Physics.* [S0034-6748(97)01606-7]

I. INTRODUCTION

Low-angle elastic light scattering (LAELS) is one of the most useful techniques to study physical and chemical systems that present inhomogeneities on length scales of the order of the wavelength of light, or larger. Maybe the most important features of LAELS are the very large range of accessible angles (~ 2 decades) and the extremely large length scales (hundreds of microns) which can be probed. These characteristics make LAELS a unique tool for studying many mesoscopic disordered systems. Examples can be found in the fields of colloidal aggregation, polymer blends, gel formation and, in general, in the chemical physics of complex fluids and critical phenomena. LAELS allows the determination of fundamental parameters such as the fractal dimension of aggregating clusters, the crossover length of gels, or the correlation length of a critical system undergoing a phase transition. It is also suitable to investigate the kinetics of many irreversible growth processes, and this is very important to elucidate the close links between the structure of the resulting system and the modalities of growth. A review of the recent experimental work carried out by using scattering techniques can be found in Ref. 1 and references therein.

But LAELS is not only of interest for basic research. It is also profitably used in many fields of applied science, such as in atmospheric and aerosol science, or for emulsions and powder characterization. Here the interest for LAELS relies on its capability to perform particle sizing.[2] Indeed, LAELS is probably one of the most convenient techniques to recover the particle size distribution of the investigated sample, the characterization being carried out *in situ* and almost in real time. As a consequence, LAELS finds application in many industrial situations and, nowadays, commercial instruments are even available on the market.

In the theory of elastic (or classical) light scattering, the light scattered out of the incident beam is due to the presence of local fluctuations of the dielectric constant ϵ of the medium. If $\langle \delta\epsilon(\mathbf{r},t)\delta\epsilon(0,t)\rangle$ indicates the spatial correlation function of such fluctuations, the intensity distribution of the scattered light is a function of the Fourier component of such correlation function and is given by[3]

$$I(\mathbf{q}) \sim \int \langle \delta\epsilon(\mathbf{r},t)\delta\epsilon(0,t)\rangle e^{i\mathbf{q}\cdot\mathbf{r}} d\mathbf{r}, \tag{1}$$

where $\langle .. \rangle$ means ensemble average or, in the case of ergodic systems, time average. The term $\mathbf{q}$ is known as the scattering wave vector and is equal to the difference between the scattered wave-vector $\mathbf{k}$ and the incident wave-vector $\mathbf{k}_0$, i.e., $\mathbf{q}=\mathbf{k}-\mathbf{k}_0$. In Eq. (1) the medium has been supposed to be isotropic (ϵ is a scalar) and the incident electric field to be linearly polarized and orthogonal to the scattering plane (the plane defined by $\mathbf{k}$ and $\mathbf{k}_0$). The magnitude of $\mathbf{q}$ is related to the scattering angle θ (the angle between $\mathbf{k}$ and $\mathbf{k}_0$) by the relation

$$q = \frac{4\pi n}{\lambda} \sin\left(\frac{\theta}{2}\right), \tag{2}$$

where λ is the vacuum wavelength of the light and n is the refraction index of the medium. Equation (1) shows that a sinusoidal fluctuation $\delta\epsilon$ described by a wave-vector $\mathbf{q}_0$ ($\delta\epsilon \sim e^{i\mathbf{q}_0\cdot\mathbf{r}}$) gives a contribution to the scattered intensity only in the direction which corresponds to $\mathbf{q}_0$. Correspondingly, by measuring the intensity scattered in that direction, it is possible to recover the amplitude of the correlation function of the dielectric constant fluctuations with length scale $\Lambda = 2\pi/q_0$ and direction parallel to $\mathbf{q}_0$. In a LAELS experiment, where the angles are so small that $\sin(\theta) \sim \theta$, this length scale is given by $\Lambda \sim \lambda/\theta$. Thus, since typical angular ranges accessible with LAELS are between 0.1° and 10°, length scales from a few microns up to hundreds of microns can be probed.

The detectors most commonly used in LAELS experiments are either annular arrays of photodiodes or charge coupled device (CCD) sensors. They have different characteristics and are to some extent complementary. The first ones are usually made of annular arrays of photodiodes with a tiny hole in the center to handle the transmitted beam. They have the advantage of requiring a very simple optical layout which is realized, in the most common configuration, by shining a collimated beam onto the sample, collecting the scattered light with a Fourier lens, and placing the sensor in the focal plane of such a lens.[4] Thus, each ring collects the light scattered at a given angle while the transmitted beam,

being focused into the tiny hole, can pass clear the sensor without affecting the measurement. Another advantage of this type of sensor is the large dynamic range and linearity which are those typical of photodiodes, i.e. $\sim 6-7$ decades, or larger. Their main limitations are the low sensitivity and the low spatial resolution. Consequently, each ring collects the light scattered over a large number of coherence areas, and this restricts their use only for static but not dynamic light scattering. Finally, a secondary but not irrelevant limitation is due to the fixed size and arrangement of the annular elements of the sensor. This imposes one to study only isotropic samples (where the intensity depends only on $|\mathbf{q}|$), and also does not leave any flexibility on the q-spacing and angular accuracy.

Conversely, CCD sensors are much more flexible detectors whose technology has grown rapidly during recent years. They are faster and much more sensitive as well. They also have a very high spatial resolution (pixel sizes are currently $\sim 10\ \mu\text{m} \times 10\ \mu\text{m}$) and, therefore, allow a very high angular resolution. This is a great advantage, since it makes it possible to use them for dynamic low-angle light scattering.[5] The main limitation of a CCD sensor is its reduced dynamic range. Indeed, if the sensor is operating at room temperature, the principal source of noise is the dark current, and this limits the dynamic range to $\sim 2-3$ decades. Another drawback is, apparently, the difficulty in devising an efficient optical scheme to perform LAELS measurements. Indeed, in the most common configuration,[6] the scattered light is forwarded onto a screen where a tiny hole allows the beam to pass clear, avoiding the transmitted beam from reaching the sensor. The intensity distribution is then measured by imaging the screen onto the CCD sensor. This scheme is fairly simple, but extremely inefficient, since most of the scattered light is lost onto the screen. To our knowledge, there are a few other detection approaches, based on optical fibers detection[7] or on off-axis parabolas and CCD,[8] but they are fairly uncommon.

In this work a CCD based LAELS instrument with a novel detection optics layout is proposed and discussed. In this scheme the light scattered by the sample is brought directly to the CCD sensor without any screen in-between. The transmitted beam is removed from the optical axis by a tiny mirror placed in the focal plane of the lens which collects the scattered light. A second lens makes the image of the plane containing the mirror on the CCD sensor plane, realizing a one-to-one correspondence between scattering angles and pixel positions. A particular arrangement of the optical elements allows one to avoid any vignetting problem, i.e. it ensures that *all* the light scattered by the sample within the detectable angular range is actually brought to the CCD sensor. The calibration of the instrument is quite easy and can be carried out by using single pinholes. The instrument sensitivity, linearity and accuracy can be easily tested and estimated with pinholes as well. Experiments on diluted suspensions of latex spheres show that the instrument also works fairly well with real samples. The results of all these tests show that the angular detection range of the instrument is ~ 2 decades, from $\sim 0.1°$ to $\sim 10°$, and that its dynamic range and linearity are both of ~ 3 decades. They also show that the performances of the instrument are actually limited by the CCD performances, implying that they could be significantly improved by simply using a better camera, such as a cooled 16 bit CCD.

II. EXPERIMENTAL SETUP

The general layout of the experimental setup is sketched in Fig. 1. The light source is a 1.5 mW He-Ne, linearly polarized, with $\lambda = 0.6328\ \mu$m and a beam size at $1/e^2$ of 0.65 mm. The beam can be stopped by an electromechanical shutter (Vincent Associates, model LS6T) which has a rise time of 0.2 ms and a minimum exposure time of 2 ms. The shutter and its exposure time are controlled by the computer via an analog-digital (AD) multifunction I/O board (National, model PC-Lab+). A variable attenuator made of a $\lambda/2$ plate and a Glan-Thompson polarizer can reduce the beam power up to a factor 10^6 and sets the polarization of the electrical field in the vertical direction (parallel to the plane of the page of Fig.1). The angular position of the $\lambda/2$ plate, and therefore the attenuation, is controlled by computer via a stepping motor. The beam is then spatially filtered, expanded to a diameter of $2w_0 = 2.5$ mm, and shined onto the sample which is contained in a square glass cell, 20 mm wide and, typically, 0.5 cm long. The power impinging on the sample is monitored by forwarding a reflection of the beam from the collimating lens onto the photodiode PD_1.

The schematic diagram of the detection optics is reported in Fig. 2. The light scattered by the sample is collected by the lens L_1 (Achromat F=80 mm, $\phi = 50$ mm) and forwarded onto the CCD camera. A filter with an optical density of 2.4 was placed in front of the CCD lens L_2. The lens L_2 (a standard photographic objective, Nikon, 50 mm, f/1.2) conjugates the plane of the CCD sensor and the focal plane of the collecting lens L_1 with a magnification ratio $M = Q_2/P_2$ ($Q_2 = 315$ mm, $P_2 = 59.4$ mm, $M = 5.3$). Therefore, a one-to-one mapping between the intensity of the light scattered at different angles and the signals out from the corresponding pixels is realized. A mirror, made of a 1.5 mm drill tip cut and polished at 45°, is placed in the focal plane of the lens L_1 and deviates the transmitted beam to 90° onto a photodiode PD_2, preventing unscattered light from reaching the CCD sensor. The drill tip is positioned so that the focused transmitted beam hits the tip very close to the upper edge, allowing light scattered at very low angles ($< 0.10°$) to pass clear. By using the signals out of the two photodiodes it is possible to recover the sample turbidity. To avoid vignetting problems associated with the lens L_2, the scattering cell is placed at a distance from the lens L_1 so that the cell plane and the L_2 plane are conjugated via the L_1 lens. In this way the spot of the scattered light onto the L_2 plane is equal to $2w_0(P_1/Q_1) \sim 10$ mm ($2w_0 = 2.5$ mm, $P_1 = 395$ mm, $Q_1 = 100$ mm), and all the light collected by the lens L_1 is also collected by the lens L_2.

To minimize stray light just simple and standard precautions were taken: the scattered light was collected only from the half plane above the mirror post; all the optics along the beam and the external surfaces of the scattering cell were antireflection (AR) coated; the cell was slightly tilted with respect to the optical axis to avoid beam reflections from

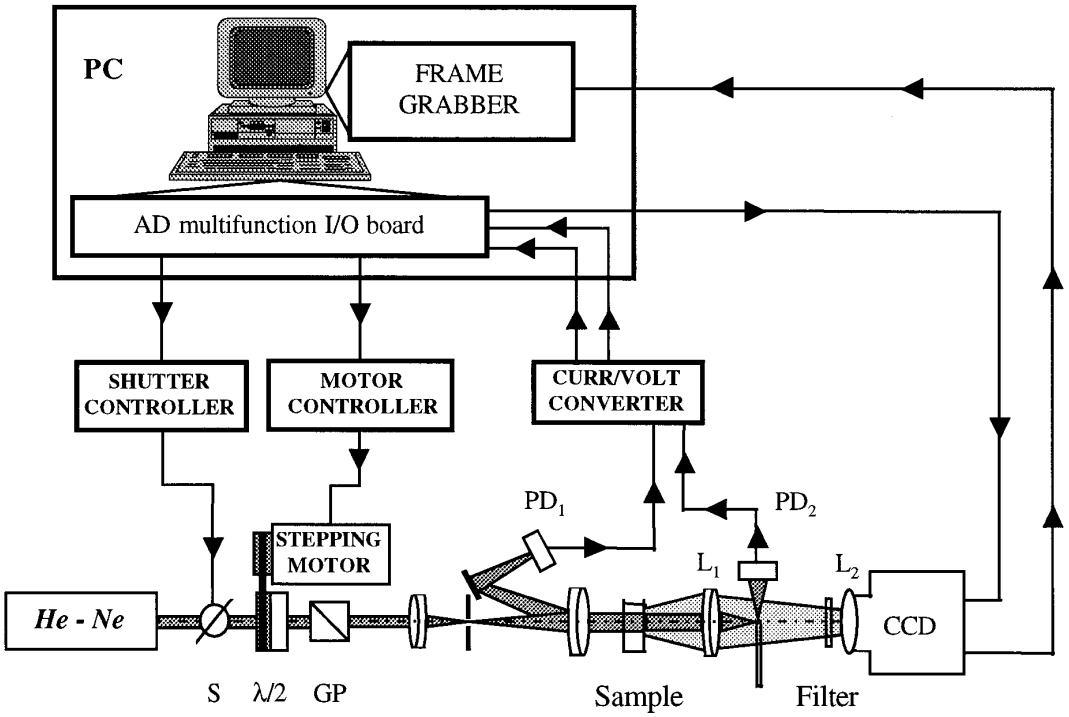

FIG. 1. Schematic diagram of the general layout of the instrument.

falling onto the CCD sensor; the cell was mounted on an X-Y micropositioner to choose the right spot for the laser beam; the filter in front of the CCD camera was an absorption filter rather than a reflection filter to avoid strong reflections backwards on the optical axis; finally the whole instrument was placed under a liftable wooden box to ensure the maximum darkness during the measurement.

The CCD camera is a variable scan, noninterlaced, full frame transfer Dalsa, model CA-D2, operating at room temperature. The pixel matrix is square with 512×512 pixels, 10 μm$\times$10 μm in size, and 100% filling ratio. The video signal out of the camera is acquired and digitized by an 8 bit frame grabber (Imaging Technology, model MFG) and the image is processed by means of a home developed software, as described below. The time necessary to processed an image is $\sim$15 s on a PC with a 100 MHz Pentium processor. The timing between the CCD, frame grabber and shutter is provided by the AD multifunction I/O board which also drives the stepping motor and digitizes the signals out of the two photodiodes PD_1 and PD_2.

The optical axis was determined by removing the mirror in the focal plane of L_1 and shining the laser beam directly

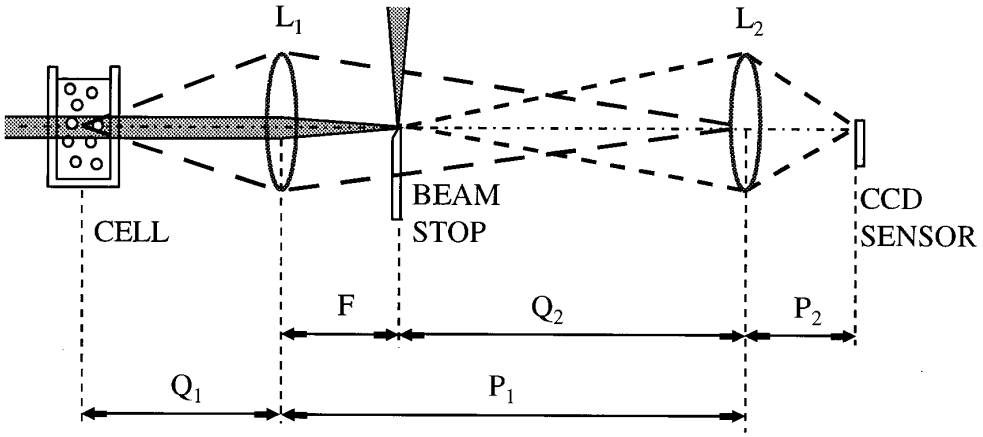

FIG. 2. Sketch of the detection optics of the instrument. The beam stop is placed in the focal plane of the lens L_1. The plane of the CCD sensor and the focal plane of the lens L_1 are conjugates via the L_2 lens. Thus, a one-to-one mapping between scattering angles and pixel positions on the CCD sensor is realized. To avoid vignetting problems associated to the L_2 lens, the cell plane and the L_2 plane are conjugated via the lens L_1.

onto the CCD camera. The beam power was attenuated by a factor $\sim 10^9$ and the corresponding image was acquired with an exposure time of 10 ms. In this way it was possible to determine the optical axis with an accuracy better than a pixel. By taking into account the size of the incident beam and the geometry of the detection optics, it is possible to estimate the average number of speckles falling on each pixel. Indeed, since the average size of a speckle is equal to the size of the transmitted beam (~ 5 μm on the CCD sensor plane), it turns out that there are ~ 4 speckles/pixel.

By referring to Fig. 2, the light scattered at an angle θ is mapped by the lens L_1 into a ring of radius $r' = F \tan\theta$ placed in the focal plane of the lens L_1 whose focal distance is F. This ring is then mapped by L_2 into a ring on the sensor plane of radius $r = r'/M$, where $M = Q_2/P_2$. Therefore, the light scattered at an angle θ is mapped on the CCD sensor into a ring of radius $r = (F/M) \tan\theta$. By using Eq. (2), it is straightforward to show that the correspondence between the wave-vector q associated to the scattering angle θ and the CCD pixels at a distance r from the optical axis, is given by

$$q = \frac{2\pi}{\lambda}\left(\frac{rM}{F}\right). \tag{3}$$

Equation (3) has been obtained by approximating $\sin\theta \sim \theta$ and by taking into account the refraction of the light exiting the scattering cell. Note that the increase of the scattering angle due to such refraction is canceled out by the reduction of the laser wavelength in the medium, leading to an expression of q independent on the refraction index of the medium.

The images were processed by dividing the pixel matrix in concentric rings centered on the optical axis so that each ring corresponds to a single q as given by Eq. (3). To allow a wider range of the detectable angles, the camera was positioned so that the optical axis falls close to one corner of the pixel matrix. Therefore only quarters of rings were considered to recover the scattered intensity distribution. In this configuration, the smallest ring has a radius $r_{min} \sim 3$ pixels corresponding to $q_{min} \sim 2.1 \times 10^2$ cm^{-1}, while, for the largest ring, $r_{max} \sim 400$ pixels, with $q_{max} \sim 2.7 \times 10^4$ cm^{-1}. Correspondingly, the scattering angles in air are $\theta_{min} \sim 0.10°$ and $\theta_{max} \sim 10.6°$. Typically, 50 concentric contiguous quarters of rings were used to fill the area between r_{min} and r_{max}. Although the ring arrangement is rather arbitrary and can be optimized depending on the sample being studied, it is often convenient to choose them by scaling their average radius $\langle r_i \rangle$ and thickness δ_i according to a geometrical progression. This implies that, with the exception of the smallest rings, $\delta_i/\langle r_i \rangle$ is a constant, with consequent equal accuracies on scattering angles and wave vectors, i.e. $\delta\theta_i/\langle \theta_i \rangle = \delta q_i/\langle q_i \rangle \sim 11\%$. In this configuration the smallest ring collects ~ 2 pixels and ~ 8 speckles, whereas in the largest ring there are $\sim 2.4 \times 10^4$ pixels and $\sim 10^5$ speckles.

If the intensity distribution presents only marginal interest at low q, but more angular accuracy is requested at large angles, the rings can be scaled linearly so that their thickness is constant over the entire matrix. In this case, the first ring is much larger with ~ 66 pixels and $\delta q_i/\langle q_i \rangle \sim 130$, whereas the last ring includes ~ 5000 pixels with $\delta q_i/\langle q_i \rangle \sim 2$. Obviously, any combination of the two spacing or any other arrangement of the rings can be selected and easily implemented, the only limitation being imposed by the pixel size. Indeed, the ultimate angular resolution of the instrument is determined by the angular aperture corresponding to the dimension of a pixel, i.e. $\delta\theta \sim (M/F)\delta r$, ~ 0.7 mrad.

III. IMAGE ELABORATION AND CORRECTING FACTORS

In the elastic light scattering theory, the intensity scattered by the sample is related to the spatial correlation function of the dielectric constant fluctuations by Eq. (1). However, from an experimental point of view, it is often more convenient to write the intensity in terms of the scattered power per unit solid angle $dP/d\Omega$. Then one has[3]

$$\frac{dP}{d\Omega} = R(\theta)\sin^2\phi \;\; P_0 \;\; L, \tag{4}$$

where P_0 is the incident power, L is length of the scattering volume, $\sin^2\phi$ is the dipole term which accounts for polarization effects, ϕ being the angle between the polarization of the incident electric field and the direction of observation, and $R(\theta)$ is known as the Rayleigh ratio. $R(\theta)$ depends on the scattering angle θ only (or on q only) and is the quantity to be recovered from the experiment.

A measure of the angular distribution of the light scattered by the sample is carried out by acquiring the image for a given exposure time and subtracting its corresponding dark image taken with the same exposure time immediately after or before the sample image. Then the signals out of the pixels belonging to the same ring are averaged and normalized by the product of the exposure time and incident laser power, providing an intensity distribution independent of the energy falling onto the CCD detector. These are the so-called *raw data*. Since stray light always affects to some extent any LAELS measurement, its contribution has to be subtracted from the sample signals. Operatively, an image with the cell filled with the solvent only is acquired and the blank raw data are worked out following the same analysis of the sample raw data. Then, since both the scattered and the stray light are attenuated by the same factor when passing through the scattering sample, the blank raw data are reduced by a factor equal to the beam attenuation, and finally subtracted from the sample raw data.

The corrections to be applied to the already blank-subtracted raw data are of different types, depending on both sample characteristics and geometrical factors. The first correction is due to the sample turbidity and takes into account the attenuation of the scattered light along the sample. Since in our geometry the scattered light is collected by the whole sample lying along the laser beam (differently from the more common cylindrical geometry where the light is collected only from the center of the cell), there are different paths for photons scattered at different angles. Therefore the correction factor depends on the scattering angle and, in the limit of $\theta \to 0$, is given by $\sim e^{\tau L}[1 - \tau L\theta^2/4]$, where τ is the sample turbidity and L is the length of the cell. However, even at very high turbidities, this is essentially a constant correction factor equal to $e^{-\tau L}$ which does not produce distortions in the

angular intensity distribution, but accounts only for absolute intensity measurements (indeed $\tau L\theta_{max}^2/4 \sim 1\%$ for $\tau L=1$).

The second correction is due to the actual acceptance solid angle associated to each scattering angle θ. If we denote with A the area of the ring associated to θ and with R its distance from the sample, the nominal solid angle associated to this ring is $\Delta\Omega_{nom}=A/R^2$. The actual acceptance solid angle is $\Delta\Omega_{act}=\Delta\Omega_{nom}\cos^3\theta$ where a term $\cos\theta$ comes from the projection of the area A orthogonal to the scattering direction and a term $\cos^2\theta$ comes from the square distance R^2. The $\cos^3\theta$ accounts for $\sim 5\%$ correction at the largest angle.

The third correction is due to polarization effects. Indeed, as reported in Eq. (4), the scattered intensity per unit solid angle is proportional to the term $\sin^2\phi$, and ϕ varies from pixel to pixel within each ring. Therefore, the correction to be applied to the scattered intensity at the angle θ is the value $\langle\sin^2\phi\rangle$, averaged over all the pixels belonging to that ring. This correction depends on rings arrangement, and, in the case of quarters of rings with one of the two sides parallel to the polarization of the incident electric field, is given by $\langle\sin^2\phi\rangle \sim 1-\theta^2/2$. This is a slight correction which, for the largest angle, is of the order of $\sim 1.5\%$.

IV. INSTRUMENTAL TESTS.

This section describes the instrumental tests performed on the instrument and the procedure followed for its calibration. It also describes how to estimate the instrument sensitivity and accuracy. Because of the high sensitivity of the CCD sensor, all these tests were fairly simple and were carried out by using single pinholes. For all the tests carried out on pinholes, the filter in front of the CCD lens was removed (see Fig. 1).

A. Calibration

The calibration of the instrument was carried out by using pinholes of different sizes, from 5 μm to 200 μm. All the pinholes were tested for manufacturing defects and roundness by using a high magnification optical microscope, which also provided an estimate of their sizes with an accuracy of approximately 0.5–1 μm. The diffraction pattern of each pinhole was measured by placing the pinhole at the cell plane and centering it onto the optical axis. The mirror post was removed and the image was acquired and processed as above. For each pinhole the incident power and the exposure time were chosen so as to have the highest energy falling onto the CCD sensor without saturation. Under these conditions, depending on the pinhole size, $\sim 2-3$ secondary maxima were clearly resolved and reliably detected. The larger pinholes, whose diameters were known with accuracies $\sim 1\%$ or better (200, 100, and 50 μm), were used to determine the actual magnification of the detection optics, resulting in $M=5.30\pm 0.05$. This value of M was used to analyze the data relative to the smaller pinholes (30, 20, 10, and 5 μm) and estimate their actual diameters. The data were fitted to the theoretical function (Airy function) only in correspondence with the main lobe, and this allowed us to estimate their sizes with an accuracy of $\sim 1-2\%$, i.e. much better than that one obtainable with the optical microscope.

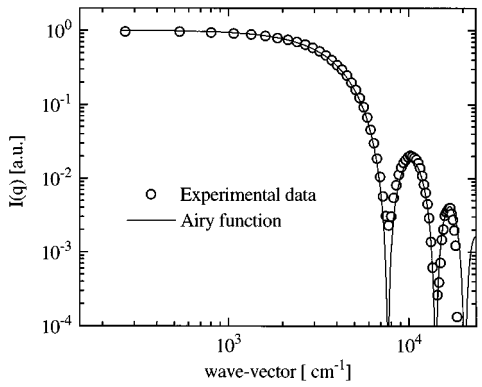

FIG. 3. Measured diffraction pattern of a 10 μm pinhole taken by shining onto the pinhole the unattenuated laser power ($P_{inc}\sim 1$ mW, $2w_o=2.5$ mm) onto the pinhole. The image was acquired with an exposure time $\Delta t_{exp}=35$ ms. The curve through the data is the Fraunhofer diffraction theory (Airy function). The data have been rescaled by an arbitrary constant so to overlap to the theoretical curve at low q's. The dynamic range of the data is ~ 3 decades.

The calibration of the instrument, both angularly and on an intensity scale, was carried out by comparing the angular positions and the intensities of the secondary maxima of all the pinholes with the corresponding theoretical values. For the angular calibration, the ratios of the positions of the theoretical to the experimental maxima of all the pinholes were reported as a function of the wave vector. By interpolating these data with a second order polynomial, we recovered a q-calibration curve that was used to correct the nominal q vectors associated to each ring. [see Eq. (3)]. For $q < 10^4$ cm^{-1}, this correction was negligible, i.e. much less than the accuracy by which the positions of the experimental maxima could be determined ($\sim 1\%$ or less), while for larger q's, it increased slowly up to $\sim 11\%$ for the largest angle. For the intensity calibration, we followed the same approach, but no corrections were necessary since corrected and non-corrected data were equal within the experimental noise.

An example of the type of measurements carried out on pinholes is reported in Fig. 3, where the diffraction pattern of a 10 μm pinhole is plotted as a function of the wave-vector q on a log-log plot. The data have been rescaled by an arbitrary constant and compared with the Fraunhofer diffraction theory. The image was acquired with the laser power not attenuated and an exposure time of 35 ms. The figure shows that the data match the theory fairly well with two secondary maxima clearly and accurately resolved. The data start to become noisy at about 3 decades below the main peak, meaning that the dynamical range of the instrument is ~ 3 decades.

B. Linearity

The linearity of the instrument with respect to the energy falling onto the CCD sensor was tested by measuring the diffraction pattern of a 20 μm pinhole. The images were acquired with different incident powers and exposure times. In Fig. 4 the intensities of main peak and the first two secondary maxima of the pinhole diffraction pattern are reported as a function of the energy falling onto the sensor.

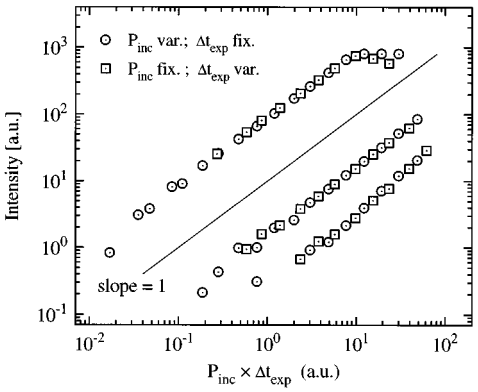

FIG. 4. Behavior of the intensities of the main peak and the first two secondary maxima diffracted by a 20 μm pinhole as a function of the energy falling onto the CCD sensor. The energy was measured by the product of the incident power P_{inc} and the exposure time Δt_{exp}. The data show a fairly good linearity over $\sim$3 decades.

The figure confirms that the dynamical range of the instrument is about 3 decades and that, within this whole range, its linearity is fairly satisfactory.

The good linearity of the instrument allows one to reliably rescale the data by the energy falling onto the sensor and compare images acquired with different incident powers and exposure times. An example is reported in Fig. 5 where the diffraction pattern of a 20 μm pinhole was measured under two different lighting conditions. The first image (circles) was acquired by sending the highest energy onto the CCD sensor without saturation ($P_{inc}=0.1P_{laser}$, $\Delta t_{exp}=30$ ms), whereas the second one (squares) was obtained by increasing the incident power by a factor 10 ($P_{inc}=P_{laser}$, $\Delta t_{exp}=30$ ms). The figure shows that both the images match the Fraunhofer diffraction theory rather accurately with an overall dynamical range of approximately 4 decades and with 4 secondary maxima accurately resolved. As a final comment, it should be noticed that, in contrast to Fig. 3, the data of Fig. 5 have been reported on a lin-log plot and are

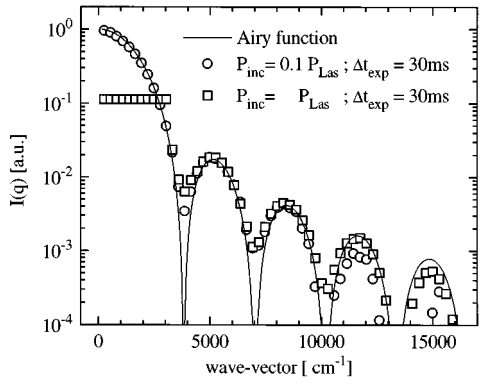

FIG. 5. Diffraction pattern of a 20 μm pinhole measured at different energies falling onto the CCD sensor. The image corresponding to the circles was acquired by choosing the incident power P_{inc} and the exposure time Δt_{exp} so to have the highest energy without saturation. The image corresponding to the squares was acquired with the incident power increased by a factor 10. Once rescaled by the product $P_{inc}\times\Delta t_{exp}$, both the images match fairly accurately the theoretical curve provided by the Fraunhofer diffraction theory (Airy function), and 4 peaks are accurately resolved. The overall dynamic range of the data is approximately 4 decades.

equidistant on the linear q scale. This shows one of the main advantages of using a CCD sensor instead of an annular array of photodiodes, whose arrangement and sizes are uniquely determined. Indeed, in this case, the images were processed by spacing the rings on a linear scale, with a consequent higher angular resolution at large q's and higher accuracy in the resolved peaks.

C. Sensitivity

The sensitivity of the instrument was estimated by measuring the absolute intensity diffracted by a pinhole. When a Gaussian beam of size $2w_0$ and incident power P_{inc} is shone on a pinhole of diameter d placed in the center of the beam, the diffracted intensity in correspondence with the zero angle falling onto the CCD sensor is given by

$$I_{diff}\sim\frac{\pi}{2}P_{inc}\frac{d^4}{(2w_0)^2\lambda^2}\left(\frac{M}{F}\right)^2, \tag{5}$$

where λ is the laser wavelength, M is the magnification of the detection optics and F is the focal length of the lens L_1 (see Fig. 2). Equation (5) has been derived supposing $d\ll 2w_0$ and neglecting all the losses due to the optics in between the pinhole and the CCD sensor (all the surfaces are AR coated). Let us analyze, for example, the data of Fig. 3 corresponding a pinhole of 10 μm. Since in that case $P_{inc}\sim 1$ mW and recalling that $M=5.3$, $F=80$ mm and $2w_0=2.5$ mm, the zero angle diffracted intensity was found to be $I_{diff}\sim 3\times 10^{-6}$ W/cm^2. By taking into account that the data become noisy at intensity levels of about three decades below the main peak, it is possible to conclude that the instrument sensitivity is of the order of $\sim 3\times 10^{-9}$ W/cm^2. Such value is reasonably consistent with the CCD nominal specifications, meaning that the instrument sensitivity is actually limited by the CCD sensitivity. Since in a room temperature operating CCD the main source of noise is due to the dark current, it is easy to infer that the use of a cooled camera (and possibly a 16-bit frame grabber) would increase the instrument sensitivity by many orders of magnitude. As a final comment, we would like to point out that such levels of intensity would hardly be detectable with a photodiode array sensor and standard electronics. Indeed, an intensity level of 10^{-9} W/cm^2 falling, for example, onto a 0.01 mm^2 photodiode, would drive a current of $\sim 4\times 10^{-2}$ pA. If this small current has to be converted into a voltage, even when very high trans-impedances (10–100 M Ω) are used, the output voltages would be fairly low, of the order of 0.4–4 μV, requiring sophisticated electronics to be used. Moreover, the use of such high impedance would drastically reduce the system bandwidth, dampening the ability of the instrument to study even slowly varying phenomena or systems under pulsed light illumination. Vice versa, in a CCD sensor the bandwidth is not related to its sensitivity and dim pulsed signals can be much more easily detected. This is of remarkable importance in many industrial applications, such as in the case of particle sizing of very diluted solutions or dispersions. Indeed, sometimes the particle concentration may be so low that one particle at a time might pass across the beam. The scattered light would then result in a stream of dim

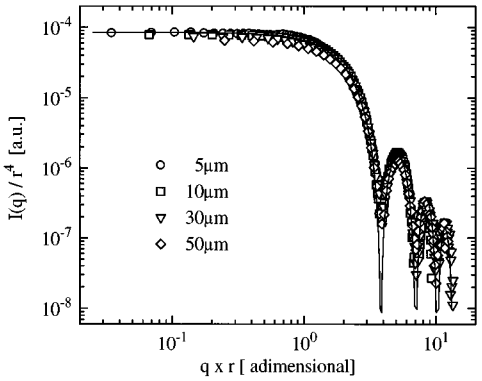

FIG. 6. Universal curve describing the intensities diffracted by pinholes of 5, 10, 30 and 50 μm diameters, normalized to the fourth power of their corresponding measured radiuses, as a function of the adimensional quantity q·r. The line through the data is the Airy function.

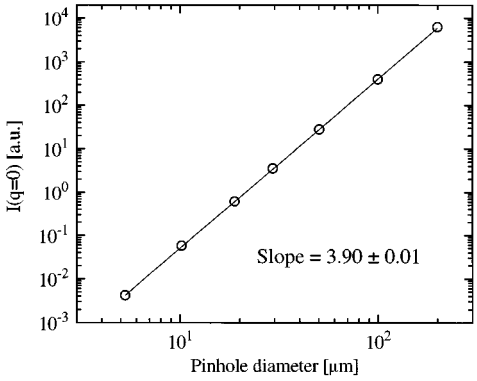

FIG. 7. Behavior of the zero angle intensity diffracted by pinholes of different sizes as a function of the pinhole diameter. The line passing through the data is the best fit with a power law function. The fitted slope of 3.90 is reasonably consistent with the value of 4 predicted by the Fraunhofer diffraction theory.

pulses randomly arriving onto the detector. In this case the photodiode array sensor would be highly unsuitable, while the CCD sensor would rather easily detect the scattered light.

D. Overall performances

The ability of the instrument to measure angular intensity distributions over the entire angular range was tested by using pinholes with diameters between 5 and 200 μm. The overall intensity dynamic range was tested as well. The procedure for the measurements of the different pinholes was the same as that followed in Sec. IV A. The Fraunhofer diffraction theory predicts that the angular distribution of the intensity diffracted by a pinhole of radius r depends only on the product q·r, and that its amplitude increases as r^4. Therefore, properly rescaling the diffraction patterns of the different pinholes, it is possible to make all the data collapse on a single universal curve. Fig. 6 shows such a curve, where the diffracted intensities of 5, 10, 30 and 50 μm pinholes, normalized to the fourth power of their corresponding measured radiuses, are plotted as a function of q·r, together with the theoretical curve (solid line). The data match with high accuracy the angular positions of the minima and maxima of the theory, but they are somewhat less accurate on the intensity scale. This is probably due to the very sensitive r^4 normalization which strongly amplifies any small percentage error on the pinhole size. The strong r^4 dependence of the amplitude of the diffracted intensity is shown in Fig. 7, where the asymptotic value I(q=0) is plotted as a function of the pinhole diameter on a log-log plot. The data exhibit a neat power low behavior with a slope $=3.90\pm0.01$, in reasonable agreement with the expected slope of 4.

V. EXPERIMENTAL RESULTS

The test of the instrument on real samples was carried out by studying aqueous suspensions of polystyrene spheres. The particle samples were from I.D.C. (Interfacial Dynamics Corporation, Portland, Oregon), with diameters between 1.78 and 6.24 μm. The sample polydispersities, as measured by means of a transmission electron microscope (TEM), were fairly narrow with standard deviations which vary, depending on particle diameter, from a few percent to about 10. All the samples were diluted in distilled water, filtered through a 0.22 μm millipore membrane and their concentrations were chosen so to have $\sim 5\%$ attenuation of the beam on a 0.5 cm cell.

As described in Sec. III, the measurements were performed by first acquiring the blank image with the cell filled with water, and secondly, by measuring the sample image. In the two measurements the cell was kept in the same position so to correctly subtract the stray light contribution from the sample scattered intensity. Figure 8 shows the intensity distributions corresponding to the two images in the case particles with nominal diameter of 6.24 μm and relative standard deviation of 10%. The sample concentration was 1.28×10^5 cm^{-3}. The images were acquired with the laser power attenuated by a factor $\sim10^3$ and the exposure time was 20 ms. The figure clearly shows the effect of the stray light. While the blank and sample data are very different over most of the entire range, they monotonically increase and become closer and closer at low q's, dampening the

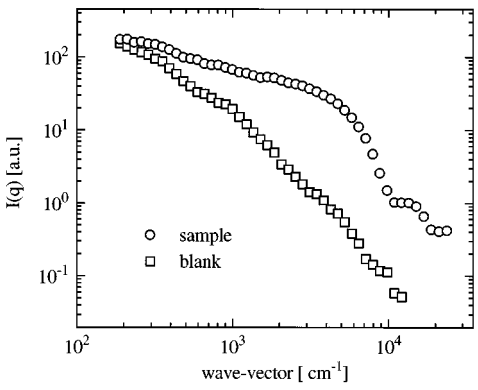

FIG. 8. Comparison between the intensity distribution as measured from a cell containing a diluted suspension of 6.24 μm-diam polystyrene spheres and the corresponding blank contribution obtained with the cell filled with water only. While the two data are quite different over most of the q-range, they become increasingly closer and closer at low q. Ultimately, it is the presence of stray light which limits the ability of measuring intensities at very low angles.

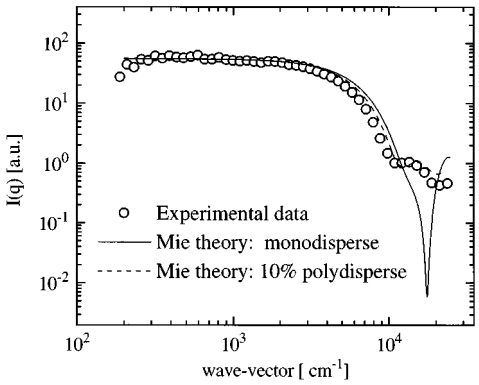

FIG. 9. Measured intensity distribution for a suspension of polystyrene spheres with an average nominal diameter of 6.24 μm and relative $\sigma = 10\%$. The data have been obtained by subtraction of the two curves of Fig. 8. The sample concentration was 1.28×10^5 cm^{-3}, so to have a ~ 5 attenuation of the transmitted beam over a 0.5 cm cell. The solid line through the data show the prediction of the Mie theory in the case of monodisperse particles with a diameter equal to the sample nominal diameter. The dashed line refers to the case of a Gaussian distribution with an average diameter and a standard deviation equal to their nominal values.

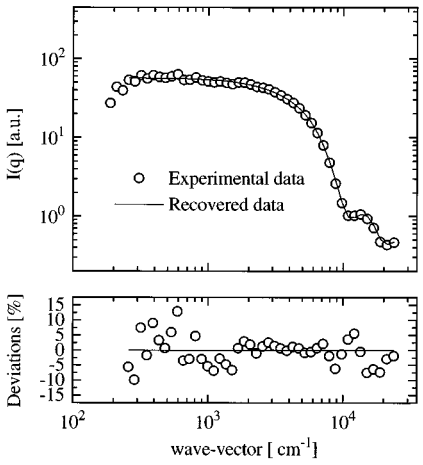

FIG. 11. Experimental data and reconstructed data obtained on the basis of the recovered distribution of Fig. 10. The data are the same as Fig. 9, with the first three at lowest q not been used for the inversion. The plot of the deviations shows a rather good matching between the experimental and reconstructed data, with rms deviations of $\sim 5\%$.

ability of the instrument to measure reliably the intensity distribution at very low angles. However, after proper subtraction of the two curves (see section III), the data exhibit a rather flat distribution as shown in Fig. 9. The two curves reported in Fig. 9 represent the predictions of the Mie theory:[9] the solid line describes the case of a monodisperse distribution with a diameter equal to the nominal sample diameter (6.24 μm); the dashed line describes the case of a Gaussian polydisperse distribution with an average diameter of 6.24 μm and a relative standard deviation equal to its nominal value, i.e. $\sigma/\langle d\rangle = 10\%$.It is evident that neither of the two curves fit the data very accurately, even if the polydisperse case is reasonably close to the data over most of the q-range. By taking into account that the particle sample distribution was recovered by TEM techniques (which are known to provide accuracies $\sim 5\%-10\%$), this mismatching is not very surprising and the data could be considered as consistent with the nominal specifications of the sample.

However, in the attempt to obtain better accuracy, we recovered the particle size distribution which allows the data to be retrieved better. The data were thus inverted by solving the classical ill posed problem

$$I(q) = \int S(q,r)N(r)dr, \tag{6}$$

where N(r) is the radius number distribution of the sample and S(q,r) is the kernel provided by the Mie theory.[9] Equation (6) was inverted by using a nonlinear iterative algorithm[10] and the results are shown in Figs. 10 and 11. Figure 10 shows the retrieved and the nominal sample distributions. The two curves are fairly similar, but the recovered one is somewhat shifted toward large radiuses, with a corresponding average diameter of 6.84 μm, $\sim 10\%$ larger than the nominal one. Its standard deviation is also slightly higher than expected, i.e. 14% against the nominal value of 10%. By recalling the above considerations about TEM accuracy, these results are reasonably consistent with the

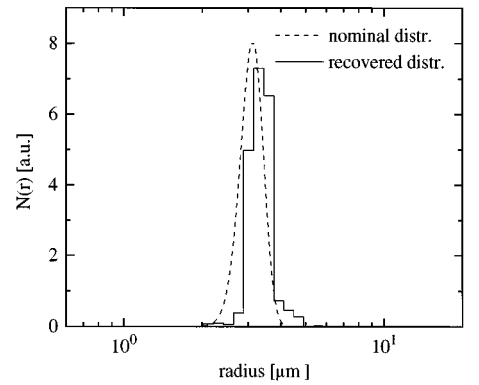

FIG. 10. Comparison between the nominal particle size distribution and the recovered one obtained by inverting Eq. (6) in the case of polystyrene spheres with an average nominal diameter of 6.24 μm and relative $\sigma = 10\%$. The data are the same as Fig. 9. The two distributions are slightly shifted with average radiuses which differ by $\sim 10\%$.

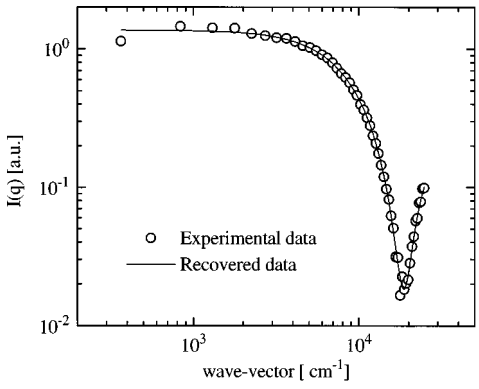

FIG. 12. Comparison between the experimental data and the reconstructed ones in the case of polystyrene spheres with an average nominal diameter of 2.75 μm and relative $\sigma = 3.4\%$. The matching between the experimental and reconstructed data are fairly good with non-systematic deviations whose rms value is $\sim 7\%$.

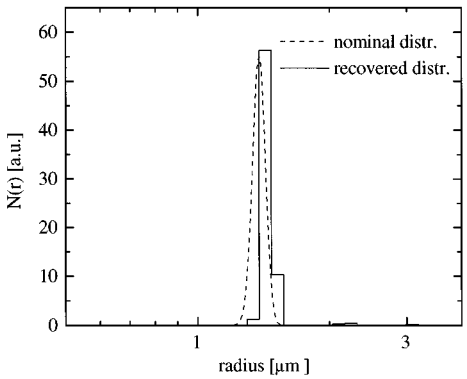

FIG. 13. Nominal particle size distribution and recovered one obtained by inverting Eq. (6) with the data of Fig. 12. The two distributions are slightly shifted with average radiuses which differ by ~7%.

sample nominal average diameter and standard deviation. The angular intensity distribution calculated on the basis of the distribution of Fig. 10 is reported in Fig. 11 (solid line) and compared with the experimental data (circles). With the exception of a few data at very low angles (which were not taken into account in the inversion), the matching between the two curves is very good over almost the entire q range. The deviations were not systematic as shown by the lower part of Fig. 11, and were of the order of 5%. The 6.24 μm sample was investigated over a variety of concentrations, from 6.54×10^4 to 3.54×10^5 cm^{-3}. In all the cases, we obtained the same results with the same levels of accuracies of those reported in Figs. 10 and 11.

As a second example of experimental data, we report in Figs. 12 and 13 the results obtained for particles with nominal average diameter of 2.75 μm and relative standard deviation of 3.4%. In this case the sample polydispersity is much smaller and a fairly deep minimum in the scattered intensity distribution is observed. Therefore, a linear spacing of the q vectors is much more suitable to accurately measure the intensity distribution. This is shown in Fig. 12, where the experimental data (circles) and the data reconstructed on the basis of the recovered distribution (solid line) are plotted together as a function of q. The two curves match very well, with no systematic deviations whose overall rms value was ~7%. The recovered distribution is shown in Fig. 13 together with the nominal one. Also in this case the two distributions are fairly similar, but slightly shifted, with average diameters which differ by ~7%.

VI. DISCUSSION

A CCD camera operating at room temperature has been used as a detector to realize a low-angle elastic light scattering instrument. A novel layout of the detection optics ensures that all the light scattered by the sample is brought directly onto the CCD sensor, without losing any of the scattered power. The optical layout allows ~2 decades in the detection angular range, from ~0.1° to ~10°. The angular accuracy depends on the specific spacing used to divide the pixel matrix. It can be optimized depending on the sample being studied, with the ultimate limit imposed by the pixel size, i.e. $\sim7\times10^{-4}$ rad. The instrument is fully controlled by a personal computer and the images can be easily processed by using a home developed software. The elaboration of an image takes ~15 s on a 100 MHz Pentium PC. The calibration of the instrument has been carried out by using single pinholes with diameters ranging from 5 to 200 μm. Single pinholes have been used to estimate the instrument sensitivity, linearity and accuracy as well. Experiments on diluted suspensions of latex spheres have shown that the instrument is fairly reliable and accurate on a real sample, too. In this case, however, systematic errors at very low angles might arise because of the presence of stray light. Thus, great care has to be taken in order to minimize the amount of stray light and correctly subtract its contribution to the scattered intensity. The results of all these tests have shown that the instrument performances are actually limited by the CCD sensor. In particular, since we have used a room temperature operating CCD camera, its dynamic range and corresponding linearity are both limited to ~3 decades. This suggests that, by using more sophisticated equipment, such as cooled CCDs and 16-bit frame grabbers, the performances of the instrument could be improved by several orders of magnitude.

As a final comment, we would like to point out that the instrument here described could easily be adapted to perform dynamic light scattering measurements, as suggested in Ref. 5. Then elastic and quasi-elastic measurements could be simultaneously carried out, providing a remarkable amount of information on the static and dynamic properties of the sample.

While we were working on the instrument described in this article, we became aware of the work done about a year ago by Tromp, Rennie, and Jones, who carried out LAELS measurements by using a CCD camera with an optical detection scheme similar to ours.[11]

ACKNOWLEDGMENTS

The author would like to acknowledge the fundamental support received by the personnel of the Istituto di Scienze Matematiche, Fisiche e Chimiche, Como, Italy. In particular, he thanks S. Grigioni for designing and machining many of the mechanical parts of the instrument, L. Martina and M. Corrias for developing a good part of the software and solving interfacing problems, A. Marelli for the contribution given during the period of her thesis, G. Righini for taking some of the measurements reported in this work, and A. Andreoni, for the overall support provided during the whole project. The author also wishes to thank L. Cipelletti, M. Giglio, Dipartimento di Fisica, University of Milan, and E. Paganini, U. Perini, C.I.S.E., Segrate, Milan, for the many helpful and illuminating discussions. A. Andreoni and E. Paganini are also thanked for the critical reading of the manuscript.

[1] *Dynamic Light Scattering*, edited by Wyn Brown (Clarendon, Oxford, 1993).
[2] *Proceedings of the Third International Congress on Optical Particle Sizing*, edited by M. Maeda, S. Nakae, and M. Ikegami (Yokohama, Japan, 1993).

[3] M. Kerker, *The Scattering of Light and other Electromagnetic Radiation*, (Academic, New York, 1969).
[4] M. Carpineti, F. Ferri, M. Giglio, E. Paganini, and U. Perini, Phys. Rev. A **42**, 7347 (1990).
[5] P. Y. Wong and P. Wiltzius, Rev. Sci. Instrum. **64**, 2547 (1993).
[6] N. Pusey, A. D. Pirie, and W. C. K. Poon, Physica A **201**, 322 (1993).
[7] A. Bailey and D. S. Cannell, Phys. Rev. Lett. **70**, 2110 (1993).
[8] W. Cumming, P. Wiltzius, F. S. Bates, and J. H. Rosedale, Phys. Rev. A **45**, 885 (1992).
[9] H. C. Van de Hulst, *Light Scattering by Small Particles* (Dover, New York, 1981).
[10] F. Ferri, A. Bassini, and E. Paganini, Appl. Opt. **25**, 5829 (1995).
[11] R. H. Tromp, A. R. Rennie, and R. A. L. Jones, Macromolecules **28**, 4129 (1995).